S. A. Brauer
Center for Advanced Vehicular Systems,
Mississippi State University,
Starkville, MS 39759
e-mail: sbrauer@cavs.msstate.edu

W. R. Whittington
Center for Advanced Vehicular Systems,
Mississippi State University,
Starkville, MS 39759
e-mail: wrw51@cavs.msstate.edu

K. L. Johnson
Center for Advanced Vehicular Systems,
Mississippi State University,
Starkville, MS 39759
e-mail: kyle@cavs.msstate.edu

B. Li
Center for Advanced Vehicular Systems,
Mississippi State University,
Starkville, MS 39759
e-mail: binli@cavs.msstate.edu

H. Rhee
Center for Advanced Vehicular Systems,
Mississippi State University,
Starkville, MS 39759
e-mail: hrhee@cavs.msstate.edu

P. G. Allison
Department of Mechanical Engineering,
University of Alabama,
Tuscaloosa, AL 35406
e-mail: pallison@eng.ua.edu

C. K. Crane
Geotechnical and Structures Laboratory,
U.S. Army Engineer Research
and Development Center,
Vicksburg, MS 39180
e-mail: charles.k.crane@usace.army.mil

M. F. Horstemeyer
Center for Advanced Vehicular Systems,
Mississippi State University,
Starkville, MS 39759
e-mail: mfhorst@cavs.msstate.edu

Strain Rate and Stress-State Dependence of Gray Cast Iron

An investigation of the mechanical strain rate, inelastic behavior, and microstructural evolution under deformation for an as-cast pearlitic gray cast iron (GCI) is presented. A complex network of graphite, pearlite, steadite, and particle inclusions was stereologically quantified using standard techniques to identify the potential constituents that define the structure–property relationships, with the primary focus being strain rate sensitivity (SRS) of the stress–strain behavior. Volume fractions for pearlite, graphite, steadite, and particles were determined as 74%, 16%, 9%, and 1%, respectively. Secondary dendrite arm spacing (SDAS) was quantified as 22.50 μm ± 6.07 μm. Graphite flake lengths and widths were averaged as 199 μm ± 175 μm and 4.9 μm ± 2.3 μm, respectively. Particle inclusions comprised of manganese and sulfur with an average size of 13.5 μm ± 9.9 μm. The experimental data showed that as the strain rate increased from 10^{-3} to $10^{3}\,s^{-1}$, the averaged strength increased 15–20%. As the stress state changed from torsion to tension to compression at a strain of 0.003 mm/mm, the stress asymmetry increased ∼470% and ∼670% for strain rates of 10^{-3} and $10^{3}\,s^{-1}$, respectively. As the strain increased, the stress asymmetry differences increased further. Coalescence of cracks emanating from the graphite flake tips exacerbated the stress asymmetry differences. An internal state variable (ISV) plasticity-damage model that separately accounts for damage nucleation, growth, and coalescence was calibrated and used to give insight into the damage and work hardening relationship. [DOI: 10.1115/1.4035616]

Keywords: high strain rate, gray cast iron, stress state, damage, structure–property relationship

1 Introduction

The most common form of cast iron, GCI, is a relatively low-price, industry-abundant material. For over 2000 years, cast iron has been used in a variety of applications ranging from kettle making [1] to automobile parts, buildings, and bridges [2]. As recently as 2005, GCI consisted of over 70% of the total casting material tonnage produced in the world, making it still an extremely relevant material for research in today's ever-expanding material society [3].

There is not much mystery as to how to control the microstructure or mechanical properties when developing a basic cast iron due to the thorough studies on cast iron over the past century. There are many discussions ranging from the effect of cooling rate on the properties of GCI [4] to more precisely what effect particular elements have on the microstructure and mechanical properties of GCI [5–7]. However, a gap in knowledge exists related to SRS under different stress states and the underlying structure-property mechanisms.

Until this project, Hsu et al. [8] had performed the only published research that took a look at the material response of GCI using a wide range of strain rates. In their study, only the modes of failure were discussed in reference to the microstructure of the

cast iron; no quantification of the microstructure or the stress-state dependence was presented. Additionally, the type of GCI as specified by ASTM A48 [9], was not made known.

Along with capturing the stress–strain behavior of a material, understanding the damage evolution in cast iron can help predict the complete material behavior by way of computer simulations. In 2000, Horstemeyer et al. [10,10] explored the damage evolution in a cast A356 aluminum showing that damage progression was driven by the initial microstructure and influenced the stress-state dependence. Damage evolution for the cast aluminum was dominated by void nucleation. Later, Jordon et al. [12] used the same technique to quantify the damage accrued during testing of a wrought 7075-T651 al alloy, and Tucker et al. [13] did the same for a wrought 6061 al alloy. These studies illustrate that for an isotropic aluminum alloy that stress asymmetries can arise due to damage progression arising differently in the different stress states. Similar studies were also completed by Allison et al. [14] for a powder metal FC-0205 steel alloy and by Whittington et al. [15] for an rolled homogenous armor steel. However, such a study has not been completed for a cast iron material.

The primary goal of the research in our study is to explore the SRS and stress-state dependence of a GCI by way of microstructure characterization and experimental testing. This understanding can then be applied to structural applications where the material may be of concern.

2 Material

Gray cast iron was chosen for this study due to its unique mechanical properties and high usage in the industry. A material that is relatively weak in tension, but strong in compression, GCI is generally characterized by its graphitic microstructure and brittle behavior during loading. This graphitic microstructure is shown in Fig. 1.

The composition of the GCI will determine whether it has a pearlitic matrix or a ferritic matrix. Pearlite provides GCI with a high modulus of elasticity and good wear resistance. Ferrite provides good thermal shock resistance and a high internal damping capacity. Both forms of GCI have good machinability and surface finish properties [16]. The chemical composition for the GCI used in this particular study yields a pearlitic matrix and is provided in Table 1.

The metallurgy of GCI is very complex and cannot be represented on the binary, iron–carbon diagram that is used in discussing steels. The reason behind this is that GCI is a ternary alloy that is composed of iron, carbon, and silicon. The carbon content of GCI is described using a carbon equivalent (CE) factor where the silicon and phosphorus contents are considered a fractional addition to the carbon and is given by the below equation

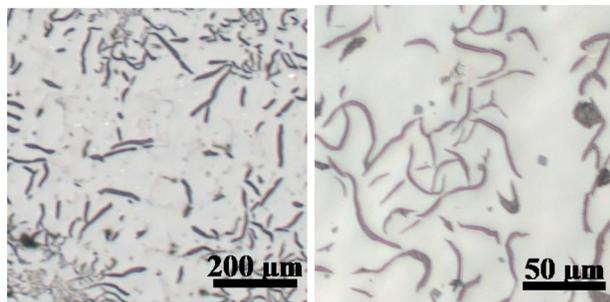$$\text{CE} = \% \text{ Total Carbon} + \frac{\% \text{ Silicon} + \% \text{ Phosphorus}}{3} \quad (1)$$

Table 1 Chemical composition of GCI (wt.%)

C	Si	Mn	P	S	Fe
3.84	1.60	0.82	0.175	0.05	Bal.

Table 2 Graphitization values of different elements as compared to silicon

	Element	Graphitization value
Graphitizers	Si	+1.00
	Al	+0.50
	Ti	+0.40
	Ni	+0.35
	Cu	+0.20
Carbide stabilizers	Mn	−0.25
	Mo	−0.30
	Cr	−1.00
	V	−2.50

The CE is an indication of how the iron solidified and thus can describe the basic microstructure of the GCI. GCI with a CE above 4.3 is considered hypereutectic. Higher strength GCI has a CE lower than 4.3 and is considered hypoeutectic.

As the gray iron begins to cool, the carbon precipitates out in the form of graphite flakes. These graphite flakes vary in length and width but ultimately are considered the weakest feature of GCI as they act similar to pre-existing cracks in the material. The formation of the graphite in the matrix can be promoted or retarded by "graphitizers" or "carbide stabilizers," respectively, and are given in Table 2 [17]. GCI is accompanied by flakes of graphite that are either uniform in distribution or grouped in rosettes, both of which are randomly oriented throughout the material matrix.

Sulfur, manganese, and phosphorus are three elements that stand out when looking at unalloyed GCI, each having some slight influence on the tensile strength. The real importance of these elements is observed as the GCI begins to solidify. The sulfur content can cause a slight increase in tensile strength but can have an equally detrimental effect on the ductility by forming iron-sulfide. Manganese is used to combine with the sulfur to prevent this formation of iron-sulfide at the grain boundaries that would otherwise cause embrittlement. These manganese-sulfide inclusions play no major role in the weakening of the material matrix. Phosphorus is used for increasing the tensile strength by forming a phase called phosphide eutectic or steadite. Steadite forms in GCI when the phosphorus content is above 0.2% and is over twice as hard as the surrounding pearlitic matrix [18]. The amount of steadite must be carefully controlled when forming GCI because the increase in steadite quickly begins to decrease the machinability. Additionally, increasing the phosphorus content above 0.4% can increase porosity in the casting depending on how solidification of the melt is controlled [17,19].

Solidification of GCI is quite possibly the most important area to control when one is looking for certain mechanical properties. Controlling solidification allows for an engineered microstructure and a sound casting. Additionally, most defects in the cast cannot be corrected by heat treating the material, adding to the importance of understanding solidification [3].

With GCI having such a complex microstructure, determining an average grain size is a very difficult task. As such, dendrite arm spacing (DAS) and SDAS have been shown to be key components in terms of the strength of GCI where SDAS is the preferred measurement over grain size [4].

The crystalline structure of GCI cannot be categorized by a single crystalline structure because of the intricate nature of its

Fig. 1 Polished GCI as observed under an optical microscope

200 µm

50 µm

Table 3 Crystalline structures and associated lattice parameters for each phase found in GCI

Crystalline phase	Crystalline structure	Lattice parameter/s (Å)	
Pearlite	α-iron (BCC)	$a = 2.87$	
	Cementite (orthorhombic)	$a = 5.06$	[37]
		$b = 6.74$	
		$c = 4.51$	
Steadite	α-iron (BCC)	$a = 2.87$	
	Phosphorus (triclinic)	N/A	
Graphite	Sheets of hexagonal lattice	$a = 2.47$	
		$c = 6.71$	
Particles	Mg (BCC)	$a = 8.89$	
	Sulfur (orthorhombic)	$a = 10.46$	[38]
		$b = 12.87$	
		$c = 24.49$	

microstructure. As such, Table 3 provides a brief overview of the various crystalline structures that are associated with the phases of the GCI that were studied. The lattice parameters were not readily available in the literature for phosphorus and thus are not provided.

3 Material Characterization

3.1 Optical and Scanning Electron Microscopy. Optical microscopy (OM) was performed using an Axiovert 200 M MD microscope. The sample microstructure that was presented in Fig. 1 was prepared using the recommended ASTM E3-01 Standard [20]. To mount the samples for polishing, each specimen was placed into a hot-mount resin. Polishing of the samples was carried out using a standard procedure recommended in the ASM Handbook [21]. Etching was performed using 2% and 4% nital on the polished specimens to reveal the secondary dendrite arms and pearlitic matrix, respectively. For direct comparison of the microstructure of the untested and tested samples, a Zeiss Evo 50 scanning electron microscope (SEM) was used with a voltage of 20 kV and a working distance of 10 mm. Electron dispersive X-ray spectroscopy (EDS) was utilized in determining the chemical composition of the particles found in the pearlitic matrix.

3.2 Hardness Testing. To classify the GCI, hardness testing was performed using a Leco LR300TD per ASTM E18-03 [22]. Per ASTM A48/A48M-03 [9], the GCI was found to be gray iron castings, ASTM A48, Class 30. The GCI that was used for testing was cast in plates of dimensions 48 in. × 48 in. × 1 in. and was provided by the U.S. Army Engineer Research and Development Center (ERDC).

3.3 Quasi-Static Experiments. For low strain rate compression testing, Ø 6.35 mm × 6.35 mm cylindrical samples were tested per ASTM E9-89a [23]. Testing was carried out using an electromechanical Instron 5882 load frame in triplicate under strain control from a 1 in. Epsilon extensometer. Specimens from the transverse and planar (through thickness) sections of the material were used during testing to determine if the material behaved isotropically. An Instron 5882 load frame performed strain controlled tension experiments on dogbone specimens with a cross section 3.175 mm × 6.35 mm and a gauge length of 6.35 mm in triplicate using a 1 in. Epsilon extensometer. Torsion tests were conducted on an MTS 858 tabletop machine with Lindholm specimens [24] that had a wall thickness of 0.5 mm. The torsion tests were displacement controlled to provide a strain rate similar to the strain rates used for compression and tension ($0.001\,s^{-1}$ and $0.1\,s^{-1}$). Both tension and torsion specimens were only cut from the transverse direction of the material.

3.4 High Strain Rate Experiments. High strain rate experiments were carried out on GCI by way of Split–Hopkinson bar testing. Split–Hopkinson bar testing utilizes instrumented long slender 350 maraging steel bars, which allow for a single shock wave to propagate throughout the specimen [25]. The waves are monitored and used to deduce the specimen mechanical response during the impact loading. For a good review of the testing methodology, the reader is referred to the study by Gama et al. [26]. For compression testing, Ø 6.35 mm-cylindrical samples, with an L/D ratio of 0.5, were tested at a strain rate of approximately $1600\,s^{-1}$. Miniature flat dogbone specimens were machined with a gauge length of 5 mm and cross section of 2 mm × 1 mm for testing the tensile response.

The high strain rate torsion tests were performed using a direct torsion Hopkinson bar and is as described by Gilat and Cheng [27]. The same Lindholm specimens [24] used for quasi-static torsion tests were used to obtain the high strain rate behavior in torsion.

4 Results and Discussion

4.1 Sample Microstructure. Both qualitative and quantitative results were produced from OM. A particular area of interest was the volume fraction of phases observed in the GCI microstructure (Fig. 2). The volume fractions were determined using a square grid systematic manual point count method as suggested by ASTM E562-02 [28]. Note that no voids were observed when determining the volume fraction of phases.

Figure 3 highlights the use of EDS in determining the composition of the particles observed throughout the pearlitic matrix. Manganese and sulfur were found to be nearly equal in the particles at 51% and 49%, respectively, and as such, are referred to as Mn/S particles hereafter.

As previously mentioned, SDAS is a key component in the strength of the material. For that reason, the SDAS was determined using the mean line intercept method that is described in ASTM E112-96(R04) [29]. A sample image used for determining SDAS is provided in Fig. 4, and the average SDAS was found to be 22.50 μm ± 6.07 μm.

Three different feature sets were explored when determining the nearest neighbor distance (NND): graphite observed by only graphite, particles observed by only particles, and graphite and particles observed by each other. The graphite-only set is clearly important due to the shape and weakness of the graphite flakes. Inclusions in the matrix are often of concern, because they can be a primary cause of weakening the microstructure and a focal point of failure. The third set clearly exhibits the smallest NND since the graphite and particles are randomly distributed throughout the microstructure. Figure 5 contains the findings for each of the feature sets along with representative images for each set.

Although the directionality of the graphite flakes was not quantified, qualitatively the graphite flakes do not appear to have a
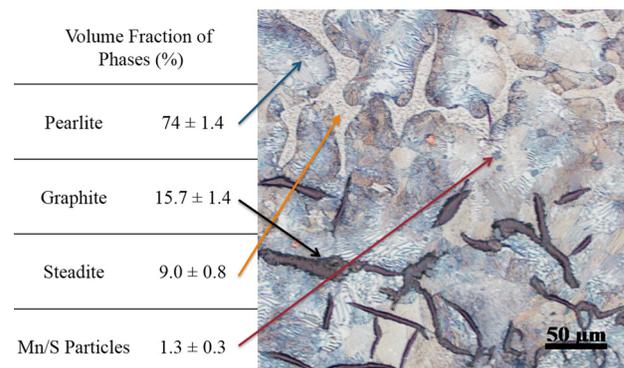

Volume Fraction of Phases (%)	
Pearlite	74 ± 1.4
Graphite	15.7 ± 1.4
Steadite	9.0 ± 0.8
Mn/S Particles	1.3 ± 0.3

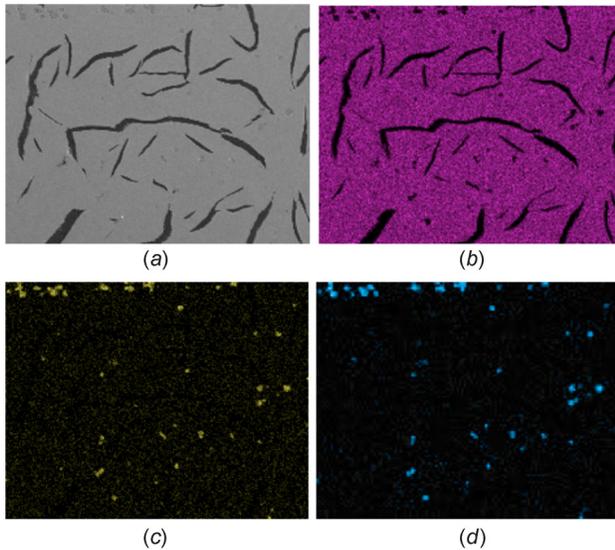**Fig. 2 Volume fraction of phases and phase identification**

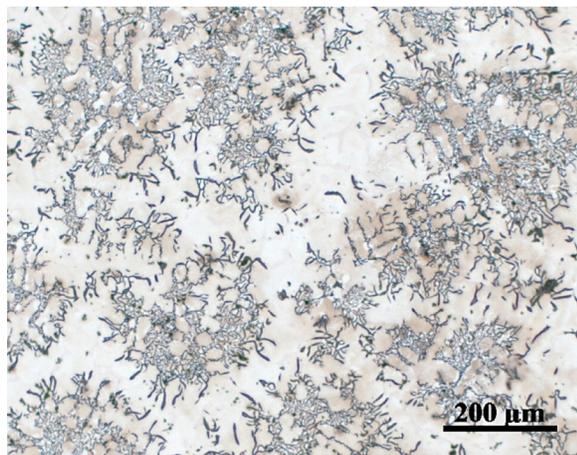Fig. 3 EDS images showing: (*a*) the original scanned image and elements, (*b*) iron, (*c*) manganese, and (*d*) sulfur

Fig. 4 Sample image used for determining SDAS (etched with 2% nital)

Fig. 5 Nearest neighbor distances when considering graphite only, particles only, and graphite and particles

preferred orientation (Fig. 6(*b*)), which can also be observed in other micrographs presented throughout this work.

Finally, the shape and size of the graphite flakes and Mn/S particles were quantified. There was a significant difference from sample to sample in terms of graphite length and width, but the
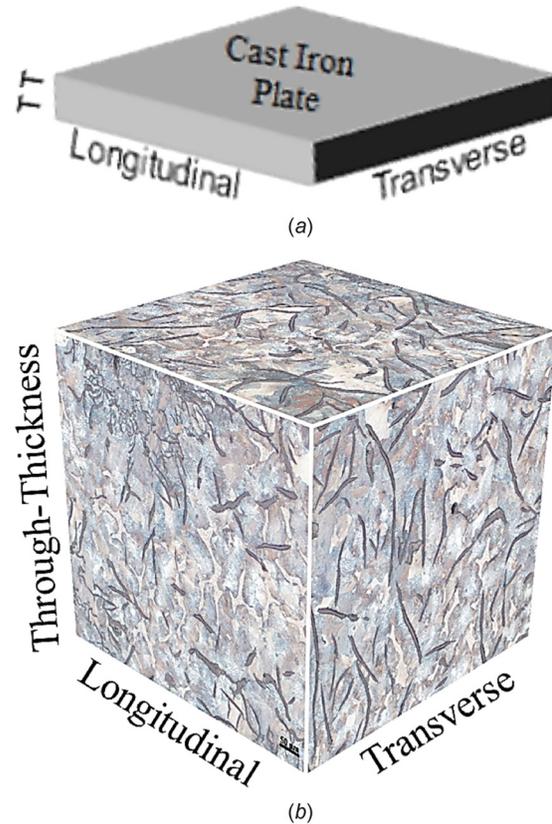

Fig. 6 (*a*) GCI plate labeled with directions used for testing and (*b*) triplanar micrograph illustrating the graphite orientations

Table 4 Graphite flake dimensions for five different samples

Flakes specimen	Size (μm^2)	Length (μm)	Width (μm)
1	1005 ± 410	167 ± 147	6.0 ± 2.8
2	971 ± 399	215 ± 181	4.5 ± 2.2
3	944 ± 363	182 ± 158	5.2 ± 2.3
4	951 ± 389	186 ± 169	5.1 ± 2.3
5	962 ± 392	247 ± 218	3.9 ± 1.8
Avg.	967 ± 391	199 ± 175	4.9 ± 2.3

Table 5 Mn/S particle dimensions for five different samples

Particles specimen	Size (μm^2)	Diameter (μm)
1	13.8 ± 10.0	4.2 ± 3.6
2	13.5 ± 9.9	4.1 ± 3.5
3	13.2 ± 9.8	4.1 ± 3.5
4	13.4 ± 9.7	4.1 ± 3.5
5	13.7 ± 9.9	4.2 ± 3.6
Avg.	13.5 ± 9.9	4.1 ± 3.5

particles did not vary so much from sample to sample. Tables 4 and 5 contain the relevant sizes and distributions for both flakes and particles, respectively. After thoroughly observing the Mn/S particles, the assumption was made that they could be treated as circular objects; therefore, a diameter was used rather than length and width.

4.2 Low and High Strain Rate Experiments. The first set of quasi-static compression tests performed was used to determine whether or not the material behaved isotropically. Specimens
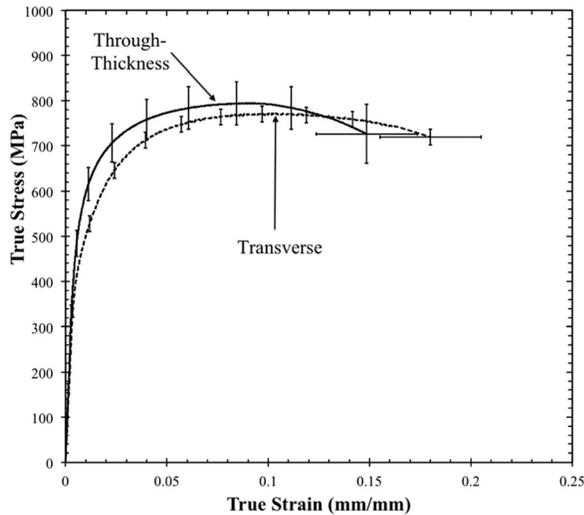
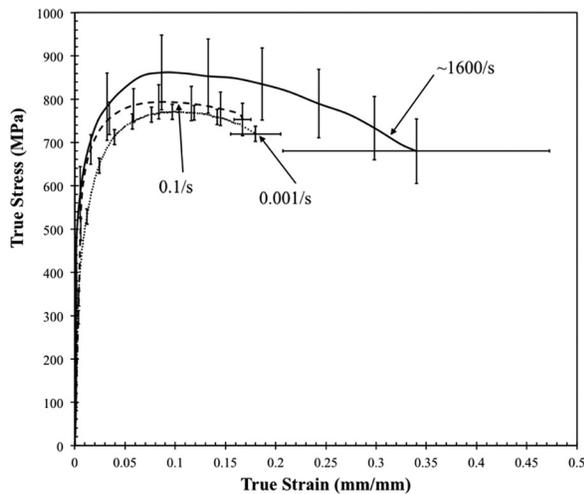**Fig. 7 Compression stress–strain behavior in the transverse and through-thickness directions at a strain rate of 0.001 s⁻¹**

Fig. 9 Stress–strain response for GCI tested in tension

Fig. 8 Compression stress–strain behavior of GCI at three different strain rates for the transverse direction

Fig. 10 Stress–strain response for GCI tested in torsion

were tested from the transverse and through-thickness directions, and the stress–strain behavior is shown in Fig. 7. With the majority of the stress–strain behavior covered by the bands of variation, the material was determined to behave isotropically. For this reason, all further testing was performed using specimens cut from the transverse direction.

The second set of quasi-static compression tests was used to observe the SRS of GCI. Figure 8 illustrates the stress–strain behavior of GCI at the two strain rates. A minor strain rate dependence was observed with the average compressive strength being 20–30 MPa higher for the GCI tested at $0.1\,\mathrm{s}^{-1}$.

Elongation to failure for each of these tests was considered at the point where the specimen could no longer maintain a load. However, the point must be made that failure of the material matrix occurs much earlier than 15–20% elongation. At the ultimate compressive strength, large cracks began to spread throughout the matrix by way of the graphite flakes. These cracks began to spread as early as 1% strain meaning that once the GCI experienced any significant strain, the material was severely weakened. This point is further accentuated in the high rate testing when examining the stress–strain response.

Figure 8 also shows the stress–strain behavior from GCI tested at $1600\,\mathrm{s}^{-1}$. Force equilibrium was achieved after 1% strain by
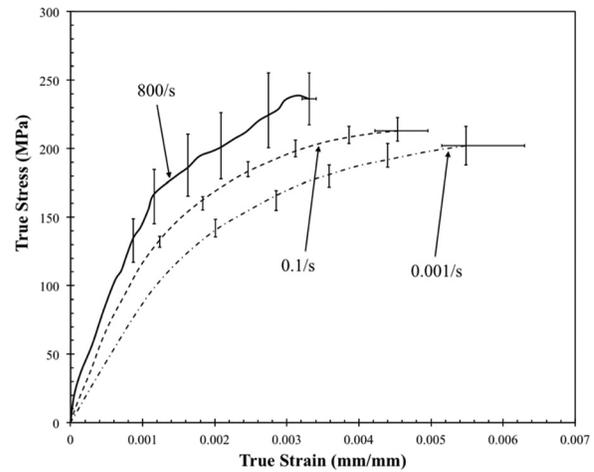
way of comparing incident and transmitted loading at the specimen sides. Unlike each of the quasi-static stress–strain curves, the failure strain of the specimen was not accurate during high strain rate experiments due to the nature of the analysis. The variation in the stress–strain behavior increased dramatically when testing at high rates. This is explained by the variation in graphite flake shape and size from specimen to specimen and the amount of energy the specimen absorbs under deformation.

Tension tests were performed at the quasi-static and high strain rates similar to the compression tests. The stress–strain behavior is shown in Fig. 9. The SRS was more apparent in tension with the average tensile strength increasing by 10% from $0.001\,\mathrm{s}^{-1}$ to $0.1\,\mathrm{s}^{-1}$ and 12% from $0.1\,\mathrm{s}^{-1}$ to $800\,\mathrm{s}^{-1}$.

Torsion tests provided different results from both the compression and tension tests. Shear stress/strains were converted to von Mises equivalent stress/strains for direct comparison to stress/strains determined in compression and tension. At strain rates of $0.0001\,\mathrm{s}^{-1}$ and $0.01\,\mathrm{s}^{-1}$, the stress–strain response was nearly identical with all tests falling within the bands of variation. High strain rate torsion tests yielded a similar response to compression and tension tests such that an overall increase in strength was observed (Fig. 10).

Due to the inherent asymmetry in the stress–strain behavior, observations of the Young's modulus for each stress state must be discussed. For the quasi-static strain rates, the modulus of
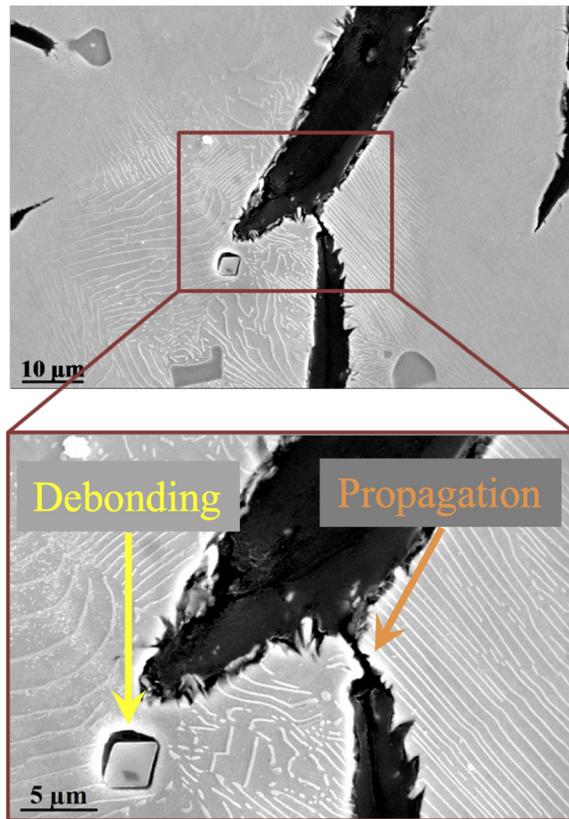
Fig. 11 Scanning electron microscope images showing crack propagation from graphite flake to graphite flake for quasi-static compression tests. Void nucleation around the particle is apparent.

elasticity for compression and torsion were found to be nearly identical. However, the elastic modulus was not found to be the same under tensile loading. The reason for this relates to the microstructure of the GCI, which presents with a relatively high amount of graphite flakes. The behavior of these flakes do not enhance the strength of the matrix under tensile loading as they act as stress concentrations and can considered as the matrix already having a preset amount of damage present, which directly affects the elastic modulus. For the high strain rates, stress-equilibrium is not achieved until $\sim$1% strain or greater, making it impossible to measure the elastic modulus.

4.3 Microstructure After Testing. The same procedure used for polishing untested samples was used for post-testing samples. Figure 11 illustrates the significance of the damage progression at the graphite spreading throughout the microstructure during quasi-static testing. The graphite flake tips acted as stress concentrations putting a great deal more stress in the local areas surrounding the tips. In Fig. 11, this stress is accentuated by the carbides that are brought out around the two graphite flakes. As mentioned previously, the Mn/S particles do not greatly affect the strength of the matrix. This point is made clear by the crack propagating from flake to flake rather than from flake to particle. Interestingly, void growth does occur around the particles in areas of high stress, which could eventually be an outlet for a propagating crack.

Figure 12 demonstrates that the damage was far more extensive in the specimens tested at the higher strain rate inducing localized void sheeting coalescence. Here, the graphite not only caused cracks to propagate, but the graphite also debonded from the surrounding pearlitic matrix. Although the stress–strain behavior proved stronger and more ductile on average, the damage imparted to the material at the higher strain rate typically yielded disintegrated samples.

Fracture surfaces from both tension and torsion at both quasi-static and high strain rates were imaged using an SEM. A trend was found between the quasi-static tension and torsion samples where the failure surfaces (Figs. 13 and 14) yielded particle clusters embedded in pearlite. Each cluster comprised 7 ± 3 particles that were an average distance of $3.1\ \mu m \pm 1.0\ \mu m$ apart. The particle clusters were found to be an average distance of $34.3\ \mu m \pm 12.2\ \mu m$ apart. Void growth around the particles was found to be relatively low as was also observed in Fig. 11 from the compression samples. The small void growth around the particles arose because the nearest neighbor distance was within four diameters. Horstemeyer et al. [30] showed that when particles or pores were within four diameters of the next particle or hole, the stress fields would interact and induce greater damage growth and was thus defined as coalescence.

High strain rate fracture surfaces for the tension and torsion samples produced a similar trend to the quasi-static results, except that particle clusters were not found; indicating that void/crack nucleation was more dominant than coalescence. Single particles were observed at an average distance of $84.3\ \mu m \pm 26.0\ \mu m$ apart, typically at the center of rosettes where the graphite had debonded (Figs. 15 and 16). Comparing the high strain rate tension to the high rate compression samples, crack propagation does occur, but in tension, debonding of the graphite from the pearlitic matrix is the main cause of failure.

4.4 Strain Rate Sensitivity and Stress-State Asymmetry. With the presence of strain rate sensitivity and stress-state asymmetry, the relationship between material microstructure and mechanical properties is imperative. The microstructure quantified and presented does not directly affect strain rate sensitivity, and as such, no relationship is garnered. The prominent feature within GCI that causes the stress-state asymmetry is the presence of graphite flakes. The flakes are considered in two ways to affect
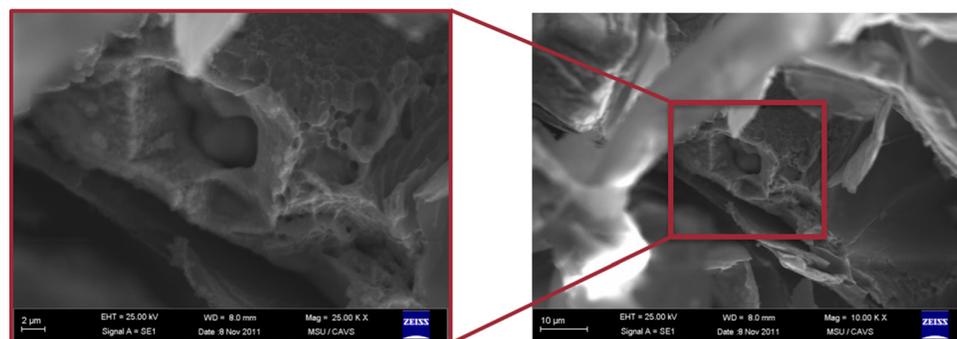

Fig. 12 Scanning electron micrograph for GCI tested at a strain rate of 1600 s^{-1} for the transverse direction showing cracks and graphite debonding
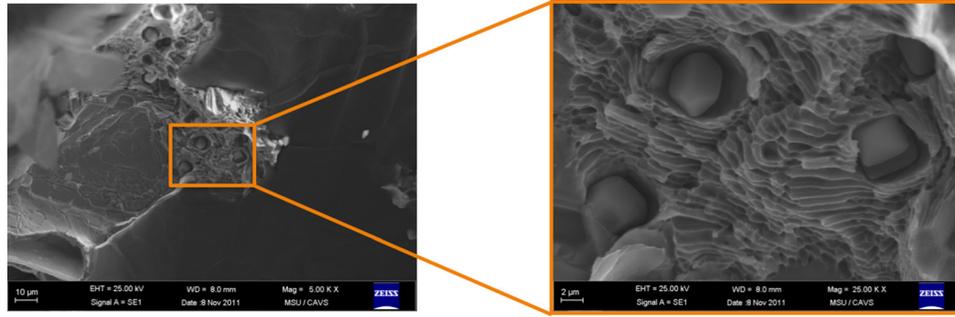
Fig. 13 Scanning electron micrograph of the failure surface for GCI tested in tension at quasi-static rates. Particle clusters were observed throughout the failure surface surrounded by the pearlitic matrix.
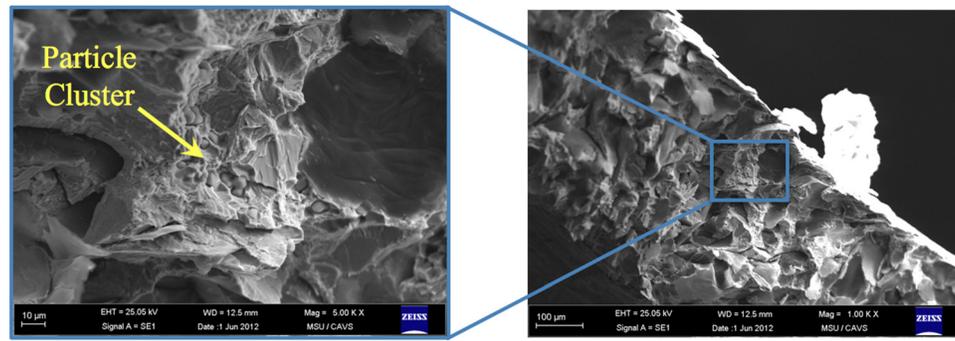
Fig. 14 Quasi-static torsion sample as seen in a scanning electron microscope. Particle clusters, shown in the enlarged image, are found throughout the fracture surface.

Fig. 15 Fracture surface for GCI tested in tension at high strain rate. Single particles were found on the fracture surface, but clusters were not evident.

Fig. 16 Fracture surface of a torsion sample tested at high rate. Debonding of graphite from the pearlitic matrix dominates the fracture surface.

Table 6 Stress values for a strain of 0.003 mm/mm

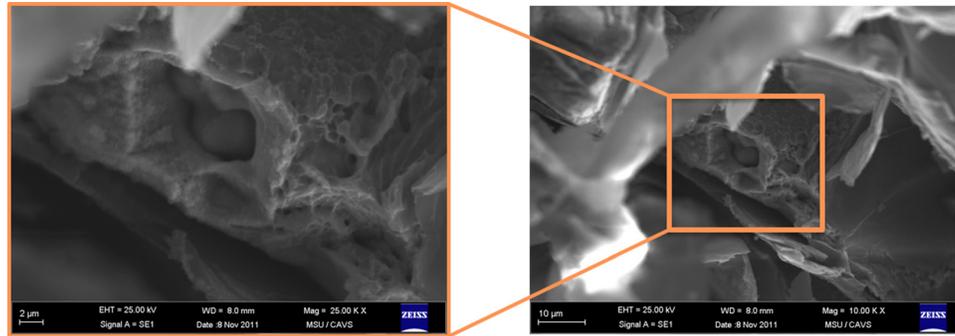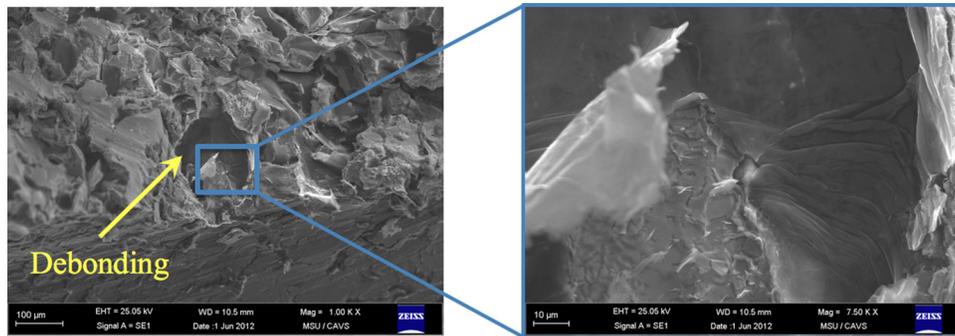| Strain rate	Compression (MPa)	Tension (MPa)	Torsion (MPa)	Stress asymmetry from torsion to compression (%)
Quasi-static ($10^{-3}\,\mathrm{s}^{-1}$)	299.6	170.2	63.3	473
High (600–$1600\,\mathrm{s}^{-1}$)	547	235.7	81.1	674
% Increase in stress	82.6	38.5	28.0	N/A

The trend here shows that not only does stress increase with strain rate, but an increase is also seen with the change in stress state from torsion to tension to compression.
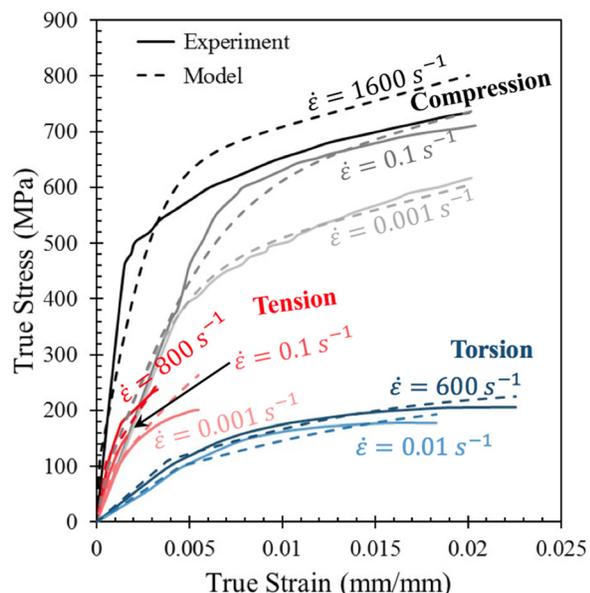

Fig. 17 Mississippi State University (MSU) ISV Plasticity-Damage model calibrated model stress–strain curves as compared to experiment stress–strain curves

the mechanical properties: (1) The long, slender shape of the flake accompanied by sharp tips provides local stress concentrations that significantly weaken the stress–strain response and (2) the flakes debond easily from the surrounding matrix, which, in tension, the matrix treats as a large void present, which affects the material not only plastically, but elastically as well.

As the strain rate increased for compression, tension, and torsion, the stress increased. The maximum increase in material strength occurred in compression, 83%, and the minimum increase in material strength occurred in torsion, 28.1%. Given the increase in strength for each stress state tested, the GCI tested is a strain rate-sensitive material.

An increase in strength also occurred as the stress state changed from torsion to tension to compression. At quasi-static strain rates, an increase in ultimate strength of 473% was found to occur as the stress state changed from torsion to compression. A similar, albeit much greater, increase was observed at higher strain rates, producing an increase in material strength of 674% when the stress state was changed from torsion to compression. In compression, even though cracks began propagating before 1% strain, the pearlitic matrix was able to maintain the load well beyond that. Under compression coalescence was inhibited thus slowing the rate of failure. In tension and torsion, coalescence of cracks emanated from the graphite flakes, dramatically increasing the total damage. The asymmetry in stress–strain behavior between stress states was influenced by the changes in coalescence between compression, tension, and torsion. Table 6 contains the relative values of stress for each stress state at a small strain of 0.003 mm/mm.

4.5 Mississippi State University ISV Plasticity-Damage Model Calibration. Special emphasis was placed on acquiring the pertinent information to understand the structure–property

Table 7 Elastic-plastic model constants for GCI determined from model calibration

ASTM A48, Class 30 GCI	Constants	Value
Elastic and thermal constants	G	40697.7
	a	0
	Bulk	83333.3
	b	0
	T_{melt}	1600
	T_{init}	298
	heat	0.34
Yield stress and adjustment constants	C_1	1
	C_2	0
	C_3	100
	C_4	0
	C_5	0.01
	C_6	0
	C_{19}	0
	C_{20}	0
Kinematic hardening and recovery constants	C_7	0
	C_8	0
	C_9	4041.96
	C_{10}	0
	C_{11}	0
	C_{12}	0
Hardening asymmetry constants	C_{13}	0.30444
	C_{14}	0
	C_{15}	78998
	C_{16}	0
	C_{17}	0.000424
	C_{18}	0

Table 8 Microstructure–property model constants obtained from model calibration

ASTM A48, Class 30 GCI	Constants	Value
Compression, tension, torsion asymmetry constants	C_a	−13040
	C_b	−1.2
McClintock void growth constants	nv	0.3
	r_0	0.06
Nucleation	a_n	10
	b_n	1100
	c_n	90
	C_{coef}	0.75
	K_{IC}	1000
	d_n	0.0046
	f_n	0.01
	NTD	0
Coalescence	cd1	0.09
	cd2	1
	dcs0	30
	dcs	22.5
	Z	1.5
	volF	0.17
	CTD	0.002
	vvfr4	0
	CAcon	0.5

relationships for GCI to calibrate an ISV plasticity-damage model [10] described in the Appendix. Data from Secs. 4.1–4.3 were used in tandem with the DMGfit routine developed by Horstemeyer et al. [31] to calibrate the MSU ISV Plasticity-Damage model. To better capture the stress–strain asymmetry observed between stress states, an expanded strain range was used for calibration of the model. Figure 17 illustrates the calibration of the model with respect to the stress–strain curves obtained from experiments. The maximum error in the calibration is 11.22%, which occurs in the $0.001 \, \text{s}^{-1}$ tension calibration curve. Constants used for calibrating the model are given in Tables 7 and 8.

5 Conclusions

Several clear conclusions can be drawn from this study:

- Compression, tension, and torsion tests at quasi-static and high strain rates were used to show that ASTM A48, Class 30 GCI is a strain rate-sensitive material. On average, the strength of the material increased by as much as 83% as the strain rate increased from 10^{-3} to 10^{3}. Large variations observed from test to test were caused by the variations in graphite from specimen to specimen.
- There exists a strong stress-state difference in the stress–strain behavior when comparing compression, tension, and torsion for this GCI. The damage progression under tension, compression, and torsion were different and this aided in the different work hardening rates as well. At quasi-static strain rates, the stress asymmetry at a strain of 0.003 mm/mm was determined to be 473% with the change from torsion to compression and 674% with the same change at high strain rates. The primary mechanism behind the asymmetry was caused by heterogeneities in the material microstructure; particularly, coalescence of cracks emanating from the tips of graphite flakes at low rates and damage nucleation at high rates.
- With the MSU ISV Plasticity-Damage model calibrated to the stress–strain behavior of GCI as well as its accompanying microstructure, a wealth of simulation-based studies are able to be performed. Any application that utilizes GCI under load-bearing conditions is capable of being analyzed. In particular, the failure of the part or structure is able to be accurately predicted even under complex loading conditions.
- Due to the large disparity between compressive and tensile behavior of the material, the mechanical response under cyclic loading is of significant interest and is considered for future work to more accurately capture the entirety of the mechanical behavior of GCI.

Nomenclature

$\underline{F}$ = deformation gradient
$\underline{F}^e$ = elastic portion of deformation gradient
$\underline{F}^p$ = inelastic portion of deformation gradient
$\underline{F}_d^p$ = isochoric inelastic portion of deformation gradient
$\underline{F}_v^p$ = volumetric inelastic portion of deformation gradient
$\underline{D}$ = rate of deformation
$\underline{D}^e$ = elastic rate of deformation
$\underline{D}^{\text{in}}$ = inelastic rate of deformation
$\underline{D}_d^p$ = isochoric inelastic rate of deformation
$\underline{D}_v^p$ = volumetric inelastic rate of deformation
J = Jacobian
V = volume
ρ = density
φ = damage or volume fraction of pores
η = pore nucleation
ν = pore growth
c = coalescence
d = average inclusion particle size

d_g = average inclusion particle size
K_{IC} = fracture toughness
f = initial particle volume fraction
J_2 = second deviatoric stress invariant
J_3 = third deviatoric stress invariant
I_1 = first stress invariant
a = constant for nucleation equation
b = constant for nucleation equation
c_2 = constant for nucleation equation
$C_{T\eta}$ = constant for nucleation equation
R_0 = initial pore radius
ε = strain
t = time
n = strain hardening exponent
m = strain rate sensitivity parameter
σ = stress
σ_h = hydrostatic stress
σ_e = equivalent von Mises stress
T = temperature
NND = pore nearest neighbor distance
d_0 = pore diameter
ζ = constant for coalescence equation
C_{TC} = temperature constant for coalescence equation
λ, μ = elastic Lame constants
G = shear modulus
$Y(T)$ = rate independent yield
$V(T)$ = strain rate dependence on yield
$f(T)$ = rate sensitivity of yield
α = kinematic hardening
h = kinematic hardening modulus
r_d = kinematic dynamic recovery
r_s = kinematic static recovery
κ = isotropic hardening
H = isotropic hardening modulus
R_d = isotropic dynamic recovery
R_s = isotropic static recovery
Y = energy release rate

Appendix

Horstemeyer et al. [11] modified the ISV plasticity model (Bammann et al. [32,33]) to account for stress-state-dependent damage evolution and to include the heterogeneities of microstructure for damage progression and failure analysis. Here, the grain size, particle size, particle volume fraction, pore size, pore volume fraction, and pore nearest neighbor distances were required within the modeling framework. The pertinent equations in this model are denoted by the rate of change of the observable and internal state variables. The equations used within the context of the finite element method are given by

$$\overset{\circ}{\underline{\sigma}} = \dot{\underline{\sigma}} - \underline{W}^e \underline{\sigma} - \underline{\sigma} \underline{W}^e$$

$$= \lambda(1 - \varphi_{\text{total}}) tr(\underline{D}^e)\underline{I} + 2\mu(1 - \varphi_{\text{total}})\underline{D}^e - \frac{\dot{\phi}_{\text{total}}}{1 - \phi_{\text{total}}} \quad \text{(A1)}$$

$$\underline{D}^e = \underline{D} - \underline{D}^{\text{in}} \quad \text{(A2)}$$

$$\underline{D}^{\text{in}} = f(T)\sinh\left[\frac{\|\underline{\sigma}' - \underline{\alpha}\| - (R + Y(T))(1 - \phi_{\text{total}})}{V(T)(1 - \phi_{\text{total}})}\right] \frac{\underline{\sigma}' - \underline{\alpha}}{\|\underline{\sigma}' - \underline{\alpha}\|} \quad \text{(A3)}$$

$$\overset{o}{\underline{\alpha}} = \dot{\underline{\alpha}} - \underline{W}^e \underline{\alpha} + \underline{\alpha} \underline{W}^e$$

$$= \left\{ h(T)\underline{D}^{\text{in}} - \left[\sqrt{\frac{2}{3}} r_d(T)\|\underline{D}^{\text{in}}\| + r_s(T)\right] \|\underline{\alpha}\|\underline{\alpha} \right\} \left[\frac{d_{g0}}{d_g}\right]^z \quad \text{(A4)}$$

$$\dot{R} = \left\{ H(T)\underline{D}^{\text{in}} - \left[\sqrt{\frac{2}{3}} R_d(T) \|\underline{D}^{\text{in}}\| + R_s(T) \right] R^2 \right\} \left[\frac{d_{g0}}{d_g} \right]^z \quad \text{(A5)}$$

$$\dot{\phi}_{\text{total}} = [\dot{\phi}_{\text{particles}} + \dot{\phi}_{\text{pores}}]c + [\phi_{\text{particles}} + \phi_{\text{pores}}]\dot{c} \quad \text{(A6)}$$

$$\dot{\phi}_{\text{particles}} = \dot{\eta}v + \eta\dot{v} \quad \text{(A7)}$$

$$\dot{\eta} = \dot{\varepsilon} \frac{d^{\frac{1}{2}}}{K_{\text{IC}}f^{\frac{1}{3}}} \eta \left\{ a \left[\frac{4}{27} - \frac{J_2^2}{J_3^3} \right] + b\frac{J_3}{J_2^{\frac{3}{2}}} + c \left\| \frac{I_1}{\sqrt{J_2}} \right\| \right\} \exp\left(-\frac{C_{\eta T}}{T} \right) \quad \text{(A8)}$$

$$\dot{v} = \frac{4}{3} \left[R_0 \exp\left(\dot{\varepsilon}\frac{\sqrt{3}}{2(1-n)} \right) \sinh\left(\sqrt{3}(1-n)\frac{\sqrt{2}I_1}{3\sqrt{J_2}} \right) \right]^3 \quad \text{(A9)}$$

$$\dot{C} = \left(\frac{4d_0}{\text{NND}} \right)^\zeta \exp(C_{\text{TC}}T)\dot{\varepsilon} \quad \text{(A10)}$$

$$\dot{\phi}_{\text{pores}} = \left[\frac{1}{(1-\phi_{\text{pores}})^m} - (1-\phi_{\text{pores}}) \right]$$
$$\times \sinh\left\{ \frac{2\left(2\frac{V(T)}{Y(T)} - 1 \right)}{\left(2\frac{V(T)}{Y(T)} + 1 \right)} \frac{\sigma_H}{\sigma_{vm}} \right\} \|\dot{\underline{\varepsilon}}\| \quad \text{(A11)}$$

The rate equations are generally written as objective rates ($\overset{\circ}{\underline{\sigma}}$, $\overset{\circ}{\underline{\alpha}}$) with indifference to the continuum frame of reference assuming a Jaumann rate in which the continuum spin equals the elastic spin ($\underline{W} = \underline{W}^e$). The ISV Eqs. (A4)–(A11) are functions of the observable variables (temperature, stress state, and rate of deformation). In general, the rate equations of generalized displacements, or thermodynamics fluxes, describing the rate of change may be written as independent equations for each ISV or as derivatives of a suitably chosen potential function arising from the hypothesis of generalized normality. An advantage of assuming generalized normality, although somewhat restrictive, is unconditional satisfaction of the Kelvin inequality of the second law of thermodynamics (nonnegative intrinsic dissipation), i.e.,

$$\underline{\sigma} : \underline{D}^{\text{in}} - \underline{b} : \overset{\circ}{\underline{\alpha}} - \kappa \bullet \dot{R} - Y_\eta \bullet \dot{\eta} - Y_v \bullet \dot{v} - Y_c \bullet \dot{c} \geq 0 \quad \text{(A12)}$$

The selection of the ISVs may, in principle, be somewhat arbitrary, but the kinematic hardening, isotropic hardening, and damage rate equations are physically motivated and strongly influence the history of the material. The ISV model accounts for deviatoric inelastic deformation resulting from the presence of dislocations in crystallographic material, dilatational deformation, and ensuing failure from damage progression.

The elastic Lame constants are denoted by λ and μ. The elastic rate of deformation ($\underline{D}^e$) results when the flow rule as shown in Eq. (A3) is subtracted from the total deformation ($\underline{D}$), which is defined by the boundary conditions that comes from the finite element analysis. The independent variables for the inelastic rate of deformation are given as the stress, temperature, and internal state variables. This is similar to power law and Garofalo [34] equations for creep except that the ISVs are now included. The deviatoric inelastic flow rule, $\underline{D}^{\text{in}}$, encompasses the regimes of creep and plasticity and is a function of the temperature, the kinematic hardening (α), the isotropic hardening (R), the volume fraction of damaged material (ϕ), and the functions $f(T)$, $V(T)$, and $Y(T)$, which are related to yielding with Arrhenius-type temperature dependence. The function $Y(T)$ is the rate-independent yield

stress. The function $f(T)$ determines when the rate-dependence affects initial yielding. The function $V(T)$ determines the magnitude of rate-dependence on yielding. These functions are determined from simple isothermal compression tests with different strain rates and temperatures

$$V(T) = C_1 \exp\left(\frac{-C_2}{T} \right), \quad Y(T) = C_3 \exp\left(\frac{C_4}{T} \right),$$
$$f(T) = C_5 \exp\left(\frac{-C_6}{T} \right) \quad \text{(A13)}$$

The kinematic hardening internal state variable, $\underline{\alpha}$, reflects the effect of anisotropic dislocation density, and the isotropic hardening internal state variable R, reflects the effect of the global dislocation density. As such, the hardening Eqs. (A4) and (A5) are cast in a hardening-recovery format that includes dynamic and static recovery. The functions $r_s(T)$ and $R_s(T)$ are scalar in nature and describe the diffusion-controlled static or thermal recovery, while $r_d(T)$ and $R_d(T)$ are scalar functions describing dynamic recovery. Hence, the two main types of recovery that are exhibited by populations of dislocations within crystallographic materials are captured in the ISVs. The anisotropic hardening modulus is $h(T)$, and the isotropic hardening modulus is $H(T)$. The hardening moduli and dynamic recovery functions account for deformation-induced anisotropy arising from texture and dislocation substructures by means of stress-dependent variables. By using J_3' in the hardening equations, the different hardening rates between axisymmetric compression and torsion (torsional softening) were accurately captured

$$r_d(T) = C_7 \left(1 + C_{19} \left[\frac{4}{27} - \frac{J_3'^2}{J_2'^3} \right] \right) \exp\left(\frac{-C_8}{T} \right) \quad \text{(A14)}$$

$$h(T) = \left\{ C_9 \left(1 + C_{20} \left[\frac{4}{27} - \frac{J_3'^2}{J_2'^3} \right] \right) \right\} - C_{10}T \quad \text{(A15)}$$

$$r_s(T) = C_{11} \exp\left(\frac{-C_{12}}{T} \right) \quad \text{(A16)}$$

$$R_d(T) = C_{13} \left(1 + C_{21} \left[\frac{4}{27} - \frac{J_3'^2}{J_2'^3} \right] \right) \exp\left(\frac{-C_{14}}{T} \right) \quad \text{(A17)}$$

$$H = C_{15} \left\{ \left(1 + C_{22} \left[\frac{4}{27} - \frac{J_3'^2}{J_2'^3} \right] \right) \right\} - C_{16}T \quad \text{(A18)}$$

$$R_s(T) = C_{17} \exp\left(\frac{-C_{18}}{T} \right) \quad \text{(A19)}$$

where $J_2' = (1/2)(\underline{\sigma}' - \underline{\alpha})^2$ and $J_3' = (1/3)(\underline{\sigma}' - \underline{\alpha})^3$. The deviatoric stress $^{\prime}$ is expressed in indicial notation as

$$\sigma_{ij}' = \sigma_{ij} - \frac{1}{3}\sigma_{ii} \quad \text{(A20)}$$

The damage variable D represents the damaged fraction of material within a continuum element. The damage reduces the material strength, enhance the inelastic flow, and soften the elastic moduli in the region where it is growing. Equations (A7)–(A11) introduces the void volume fraction (porosity) as damage. By including damage, D, as an ISV, different forms of damage rules can easily be incorporated into the constitutive framework. Bammann and Aifantis [35] demonstrated the applicability of the Cocks and Ashby [36] void growth rule used as the damage rate equation in the ISV model. In the framework above, each damage component (nucleation, η, growth, v, and coalescence, c) evolve as ISVs.

The generalized thermodynamic force conjugate, Y, is often referred to as the energy release rate for elastic brittle materials and the J-integral for inelasticity. In essence, an increment of damage will have associated energy released per unit damage extension as new damaged area (or volume) is developed.

The damage progression is divided into void nucleation and growth from second phase particles and from pores. Coalescence ISV in Eq. (A10) is introduced to reflect pore–pore interactions and particle-pore interactions. The void nucleation ISV in Eq. (A8) is discussed in length by Horstemeyer et al. [11]. The void growth ISV is related to the particles inducing pores/voids, Eq. (A9). Other forms can be used and evaluated, but this equation allows for a strain rate sensitivity in relation to the plasticity model ($m = V(T)/Y(T)$). For the porosity evolution, the Cocks and Ashby [36] void growth rule is used as shown in Eq. (A11). In these equations, the microstructural features to be used are the following: Particle size, d; volume fraction of particles, f; grain size, d_g; pore size, p; $v_{initial} = 4/3\pi(p/2)^3$, volume fraction of pores, ϕ_{pores}.

References

[1] Krause, D. E., 1969, "Gray Iron-A Unique Engineering Material, Gray, Ductile, and Malleable Iron Castings: Current Capabilities," ASTM International, Conshohocken, PA, Standard No. ASTM STP 455, pp. 3–28.

[2] Sawyer, M. H., 1979, "World's First Iron Bridge," Civ. Eng. ASCE, 49(12), pp. 46–49.

[3] Stefanescu, D. M., 2005, "Solidification and Modeling of Cast Iron—A Short History of the Defining Moments," Mater. Sci. Eng., 413–414, pp. 322–333.

[4] Jabbari Behnam, M. M., Davami, P., and Varahram, N., 2010, "Effect of Cooling Rate on Microstructure and Mechanical Properties of Gray Cast Iron," Mater. Sci. Eng., 528(2), pp. 583–588.

[5] Abbasi, H. R., Bazdar, M., and Halvaee, A., 2007, "Effect of Phosphorus as an Alloying Element on Microstructure and Mechanical Properties of Pearlitic Gray Cast Iron," Mater. Sci. Eng., 444(1–2), pp. 314–317.

[6] Fourlakidis, V., Diaconu, V. L., and Diószegi, A., 2010, "Effects of Carbon Content on the Ultimate Tensile Strength in Gray Cast Iron," Mater. Sci. Forum, 649, pp. 511–516.

[7] Slyn'ko, G. I., Grabovyi, V. M., and Volchok, I. P., 1993, "Effect of Phosphide Eutectic on the Properties of a Cast Iron Alloy," Metal Sci. Heat Treat., 35(3), pp. 155–159.

[8] Hsu, C.-H., Lee, S.-C., Wang, L., and Dong, X., 2002, "The High Strain-Rate Fracture Behaviors of Gray Iron Under Compressive Loading," Mater. Chem. Phys., 73(2–3), pp. 174–178.

[9] ASTM, 2003, "Specification for Gray Iron Castings," ASTM International, Conshohocken, PA, Standard No. ASTM A48/A48M-03.

[10] Horstemeyer, M. F., Lathrop, J., Gokhale, A. M., and Dighe, M., 2000, "Modeling Stress State Dependent Damage Evolution in a Cast Al–Si–Mg Aluminum Alloy," Theor. Appl. Fract. Mech., 33(1), pp. 31–47.

[11] Horstemeyer, M. F., Gall, K., Dolan, K. W., Waters, A., Haskins, J. J., Perkins, D. E., Gokhale, A. M., and Dighe, M. D., 2003, "Numerical, Experimental, Nondestructive, and Image Analyses of Damage Progression in Cast A356 Aluminum Notch Tensile Bars," Theor. Appl. Fract. Mech., 39(1), pp. 23–45.

[12] Jordon, J. B., Horstemeyer, M. F., Solanki, K., Bernard, J. D., Berry, J. T., and Williams, T. N., 2009, "Damage Characterization and Modeling of a 7075-T651 Aluminum Plate," Mater. Sci. Eng., 527(1–2), pp. 169–178.

[13] Tucker, M. T., Horstemeyer, M. F., Whittington, W. R., Solanki, K. N., and Gullett, P. M., 2010, "The Effect of Varying Strain Rates and Stress States on the Plasticity, Damage, and Fracture of Aluminum Alloys," Mech. Mater., 42(10), pp. 895–907.

[14] Allison, P. G., Grewal, H., Hammi, Y., Brown, H. R., Whittington, W. R., and Horstemeyer, M. F., 2013, "Plasticity and Fracture Modeling/Experimental Study of a Porous Metal Under Various Strain Rates, Temperatures, and Stress States," ASME J. Eng. Mater. Technol., 135(4), p. 041008.

[15] Whittington, W. R., Oppedal, A. L., Turnage, S., Hammi, Y., Rhee, H., Allison, P. G., Crane, C. K., and Horstemeyer, M. F., 2014, "Capturing the Effect of Temperature, Strain Rate, and Stress State on the Plasticity and Fracture of Rolled Homogeneous Armor (RHA) Steel," Mater. Sci. Eng., 594(31), pp. 82–88.

[16] Davis, J. R., and ASM International Handbook Committee, 1996, Cast Irons, ASM International, Materials Park, OH.

[17] Walton, C. F., and Society, G. I. F., 1957, The Gray Iron Castings Handbook: Including Data on Gray, Ductile (Nodular), White, and High Alloy Irons, Gray Iron Founders' Society, Cleveland, OH.

[18] Angus, H. T., 1976, Cast Iron: Physical and Engineering Properties, Butterworths, London, UK.

[19] Srivatsan, T., and Sudarshan, T., 1999, "The Influence of Phosphorus on Shrinkage Porosity in Cast Irons," Mater. Lett., 41(4), pp. 186–191.

[20] ASTM, 2001, "Guide for Preparation of Metallographic Specimens," ASTM International, Conshohocken, PA, Standard No. ASTM E3-01.

[21] Vander Voort, G. F., and ASM International Handbook Committee, 2004, ASM Handbook, (Metallography and Microstructures), Vol. 9, ASM International, Materials Park, OH.

[22] ASTM, 2003, "Test Methods for Rockwell Hardness of Metallic Materials," ASTM International, Conshohocken, PA, Standard No. ASTM E18-03.

[23] ASTM, 2000, "Test Methods of Compression Testing of Metallic Materials at Room Temperature," ASTM International, Conshohocken, PA, Standard No. ASTM E9-89a.

[24] Lindholm, U. S., Nagy, A., Johnson, G. R., and Hoegfeldt, J. M., 1980, "Large Strain, High Strain Rate Testing of Copper," ASME J. Eng. Mater. Technol., 102(4), p. 376.

[25] Staab, G. H., and Gilat, A., 1991, "A Direct-Tension Split Hopkinson Bar for High Strain-Rate Testing," Exp. Mech., 31(3), pp. 232–235.

[26] Gama, B. A., Lopatnikov, S. L., and Gillespie, J. W., 2004, "Hopkinson Bar Experimental Technique: A Critical Review," ASME Appl. Mech. Rev., 57(4), p. 223.

[27] Gilat, A., and Cheng, C.-S., 2000, "Torsional Split Hopkinson Bar Tests at Strain Rates Above 104s−1," Exp. Mech., 40(1), pp. 54–59.

[28] ASTM, 2002, "Test Method for Determining Volume Fraction by Systematic Manual Point Count," ASTM International, Conshohocken, PA, Standard No. ASTM E562-02.

[29] ASTM, 2004, "Test Methods for Determining Average Grain Size," ASTM International, Conshohocken, PA, Standard No. ASTM E112-96(R04).

[30] Horstemeyer, M. F., Matalanis, M. M., Sieber, A. M., and Botos, M. L., 2000, "Micromechanical Finite Element Calculations of Temperature and Void Configuration Effects on Void Growth and Coalescence," Int. J. Plast., 16(7–8), pp. 979–1015.

[31] Horstemeyer, M. F., Cariño, R., Hammi, Y., and Solanki, K. N., 2009, "MSU Internal State Variable Plasticity-Damage Model 1.0 Calibration, DMGfit Production Version," Mississippi State University, Starkville, MS, Report No. CAVS REPORT MSU.CAVS.CMD.2009-R001.

[32] Bammann, D. J., 1984, "An Internal Variable Model of Viscoplasticity," Int. J. Eng. Sci., 22(8–10), pp. 1041–1053.

[33] Bammann, D. J., Chiesa, M. L., Horstemeyer, M. F., and Weingarten, L. I., 1993, "Failure in Ductile Materials Using Finite Element Methods," Structural Crashworthiness and Failure, Taylor & Francis, Abingdon, UK, pp. 1–54.

[34] Garofalo, F., 1963, "An Empirical Relation Defining the Stress Dependence of Minimum Creep Rate in Metals," Trans. Metall. Soc. AIME, 227(2), pp. 351–355.

[35] Bammann, D. J., and Aifantis, E. C., 1989, "A Damage Model for Ductile Metals," Nucl. Eng. Des., 116(3), pp. 355–362.

[36] Cocks, A. C. F., and Ashby, M. F., 1981, "Creep Fracture by Void Growth," Creep in Structures, A. R. S. Ponter and D. R. Hayhurst, eds., Springer, Berlin, pp. 368–387.

[37] Chiou, W., 2003, "Structure and Stability of Fe3C-Cementite Surfaces From First Principles," Surf. Sci., 530(1–2), pp. 88–100.

[38] Meyer, B., 1976, "The Structures of Elemental Sulfur," Advances in Inorganic Chemistry, Elsevier, Amsterdam, The Netherlands, pp. 287–317.